Journal of Alloys and Compounds 877 (2021) 160171

Contents lists available at ScienceDirect

Journal of Alloys and Compounds

journal homepage: www.elsevier.com/locate/jalcom

Complex magnetic ordering in $RE_5Pd_2In_4$ (RE = Tb-Tm) compounds investigated by neutron diffraction and magnetometric measurements

Stanisław Baran[a,*], Aleksandra Deptuch[b], Manfred Reehuis[c], Yuriy Tyvanchuk[d], Fabiano Yokaichiya[c], Andrzej Szytuła[a]

[a] M. Smoluchowski Institute of Physics, Jagiellonian University, prof. Stanisława Łojasiewicza 11, PL-30-348 Kraków, Poland
[b] Institute of Nuclear Physics Polish Academy of Sciences, Radzikowskiego 152, PL-31-342 Kraków, Poland
[c] Helmholtz-Zentrum Berlin für Materialien und Energie GmbH, Hahn-Meitner Platz 1, D-14109 Berlin, Germany
[d] Analytical Chemistry Department, Ivan Franko National University of Lviv, Kyryla i Mefodiya 6, 79005 Lviv, Ukraine

ARTICLE INFO

Article history:
Received 16 February 2021
Received in revised form 22 April 2021
Accepted 24 April 2021
Available online 5 May 2021

Keywords:
Intermetallics
Magnetically ordered materials
Rare earth alloys and compounds
Magnetisation
Magnetic measurements
Neutron diffraction

ABSTRACT

The $RE_5Pd_2In_4$ (RE = Tb-Tm) compounds crystallize with the orthorhombic $Lu_5Ni_2In_4$-type crystal structure (*Pbam* space group). In this work we report results of structural and magnetic studies by means of X-ray and neutron diffraction as well as dc and ac magnetometric data. Magnetic susceptibility and neutron diffraction data revealed rare-earth moments order at low temperatures with complex magnetic structures showing a cascade of temperature-induced transitions. The magnetic ordering temperatures are found to be 97, 88, 28.5, 16.5 and 4.3 K for RE = Tb, Dy, Ho, Er and Tm, respectively. Magnetic structures related to the propagation vector $\vec{k}_1 = [0, 0, 0]$ are found just below the magnetic ordering temperatures in majority of the investigated compounds (RE = Tb-Er). Below the Curie temperature T_C they have purely ferromagnetic character in $Tb_5Pd_2In_4$ and $Dy_5Pd_2In_4$. A ferrimagnetic order finally sets at lower temperatures in $Dy_5Pd_2In_4$, while in $Ho_5Pd_2In_4$ two magnetic phases related to $\vec{k}_1$ are observed: the antiferromagnetic one (phase I) and the ferrimagnetic one (phase II, coexisting with phase I at lower temperatures). $Er_5Pd_2In_4$ is a canted antiferromagnet with additional ferromagnetic component developing at lower temperatures. A purely antiferromagnetic component of magnetic structure with enlarged magnetic unit cell appears with decreasing temperature in $Tb_5Pd_2In_4$ ($\vec{k}_2 = [0, \frac{1}{2}, 0]$ and $\vec{k}_3 = [0, \frac{1}{2}, \frac{1}{2}]$) while in $Ho_5Pd_2In_4$ such component ($\vec{k}_4 = [\frac{1}{4}, 0, 0]$) is present within whole temperature range below the magnetic ordering temperature. Magnetic structure of $Tm_5Pd_2In_4$, exceptionally, has no $\vec{k}_1$ component, but is an antiferromagnetic incommensurate one related to two propagation vectors: $\vec{k}_5 = [0.073(3), 0.451(1), \frac{1}{2}]$ and $\vec{k}_6 = [0, 0.335(2), \frac{1}{2}]$. In majority of the compounds (RE = Tb-Er) the first rare-earth 4*g* site (noted as 4*g*1) orders at lower temperature than two remaining sites (2*a* and 4*g*2). The direction of the magnetic moments depends on rare-earth element involved and indicates an influence of single-ion anisotropy in the crystalline electric field (CEF).

1. Introduction

The research in the field of magnetism of rare earth intermetallics concentrates nowadays on systems with complex crystal structures where localized magnetic moments are distributed among different Wyckoff sites. Such a distribution of magnetic moments leads to complex magnetic properties like presence of a cascade of temperature- and/or field-induced magnetic transitions, formation of complex non-collinear magnetic structures, coexistence of ferro- and antiferromagnetic components of magnetic structure, etc.

A series of ternary intermetallics of general composition $RE_5Pd_2In_4$ (RE = Sc [1], Y, Tb-Tm, Lu [2]) is a good example of such a system. The compounds are formed at 870 K and they crystallize in a complex crystal structure of the $Lu_5Ni_2In_4$-type (Pearson symbol oP22, space group *Pbam*, No. 55, $Z = 2$) [3], where the rare-earth atoms occupy three nonequivalent crystallographic positions. No magnetic data have been yet reported for the $RE_5Pd_2In_4$ compounds, except for $Sc_5Pd_2In_4$ which is found to be a Pauli paramagnet [1].

* Corresponding author.
E-mail address: stanislaw.baran@uj.edu.pl (S. Baran).

https://doi.org/10.1016/j.jallcom.2021.160171
0925-8388/

In case of the isostructural $RE_5Ni_2In_4$ system, the magnetic properties have only been determined for selected members. $Tb_5Ni_2In_4$ is a ferro-/ferrimagnet below T_C = 125 K with an additional antiferromagnetic component appearing below T_N = 20 K [4]. $Dy_5Ni_2In_4$ has been reported to order ferromagnetically below T_C = 105 K followed by a transformation to an antiferromagnetic state below T_N = 30 K [5] or 20 K [6]. $Ho_5Ni_2In_4$ orders magnetically below 31 K [4,6] or 30 K [7]. The neutron diffraction data indicate formation of an antiferromagnetic structure which transforms to a ferrimagnetic one at 25 K [4] or 19 K [6]. In $Er_5Ni_2In_4$ a long-range magnetic ordering develops below 18.5 K [8] or 21 K [6]. $Tm_5Ni_2In_4$ is a complex antiferromagnet with the Néel temperature of 4.2 K [9] or 4.1 K [10]. Recent investigation of magnetocaloric effect in $RE_5Ni_2In_4$ showed magnetic entropy changes around T_C equal to 4.7, 10.1 and 10.2 J/(kg · K) for RE = Dy, Ho and Er, respectively [6].

This work is a part of our broader study concerning magnetic properties of ternary indides. In this paper we focus on both the macroscopic (magnetic susceptibility, magnetization) as well as microscopic (crystal and magnetic structures) properties of the $RE_5Pd_2In_4$ (RE = Tb-Tm) system. The research involves different experimental techniques including magnetic measurements as well as X-ray and neutron diffraction. The obtained data are compared with those for the isostructural $RE_5Ni_2In_4$ compounds, in order to determine the influence of different transition metal elements (Ni and Pd) on the magnetic order in the rare earth sublattice.

2. Experimental details

The samples of $RE_5Pd_2In_4$ (RE = Tb-Tm) were prepared by arc-melting of high-purity metals (99.9 wt% purity for RE, 99.99 wt% for Pd and In) having total mass of about 5 g under a pure argon atmosphere. The buttons were sealed in evacuated silica tubes and annealed at 870 K for one month. Afterwards they were quenched into cold water. The crystal structure of the obtained samples was examined by X-ray powder diffraction at room temperature using a PANalytical X'Pert PRO or Empyrean diffractometer (Cu Kα-radiation, Bragg-Brentano geometry, measured angle interval $2\theta = 10 - 130^{\circ}$, step scan mode, step size in $2\theta = 0.03^{\circ}$, 15 s/step). The FullProf [11,12] program package was used for the Rietveld analysis of the collected X-ray data set.

The dc magnetic measurements were carried out on a VSM option of the Physical Property Measurement System (PPMS) by Quantum Design. The zero-field cooled (ZFC) and field cooled (FC) magnetic susceptibility vs. temperature curves were collected in a low external magnetic field of 50 Oe in order to determine temperatures of magnetic phase transitions. The ZFC magnetic susceptibility vs. temperature curves were recorded at 1 kOe in wide temperature range (1.9–390 K) in order to find the values of effective magnetic moments and paramagnetic Curie temperatures. Finally, hysteresis loops in applied magnetic fields up to 90 kOe were taken at a number of temperatures in order to find character of magnetic ordering and determine the critical and coercivity fields.

In addition to the dc magnetic measurements, the ac ones were completed with the use of an ACMS option of the Physical Property Measurement System (PPMS) by Quantum Design. The real (χ') and imaginary (χ'') magnetic susceptibility components were collected in function of temperature with the amplitude of oscillating magnetic field equal to 2 Oe. The dc component of magnetic field was fixed to zero during measurement.

Powder neutron diffraction patterns were collected on the E2 diffractometer ($\lambda = 2.381$ Å) located at the Helmholtz-Zentrum Berlin. The data were collected at a number of temperatures between 1.4 and 120 K. The Rietveld-type program FullProf [11,12] was used for processing the diffraction data.

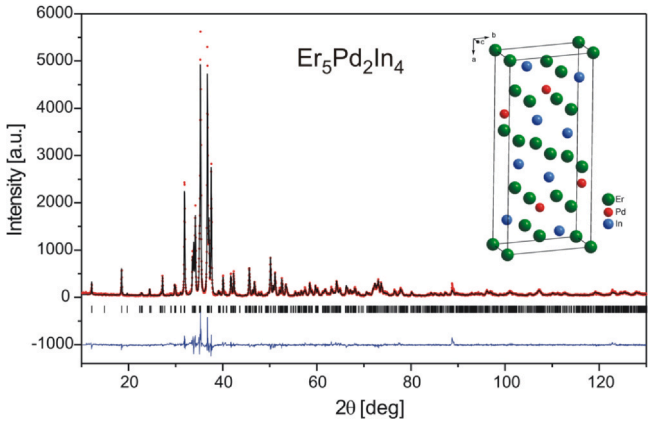

Fig. 1. X-ray diffraction pattern of $Er_5Pd_2In_4$ (Cu Kα radiation) collected at room temperature. The solid circles are for the experimental data, the line shows the result of Rietveld refinement, the vertical bars mark the Bragg reflection positions while the difference between the experimental data and the refinement is plotted at the bottom of the figure. The upper inset shows the crystal structure of $Er_5Pd_2In_4$ compound.

3. Crystal structure

X-ray powder diffraction data of the $RE_5Pd_2In_4$ samples collected at room temperature indicate that they crystallize in the orthorhombic $Lu_5Ni_2In_4$-type structure (Pearson symbol oP22, space group *Pbam*, No. 55, $Z = 2$) [3]. Fig. 1 shows, as an example, a diffraction pattern of the $Er_5Pd_2In_4$ sample with corresponding crystal unit cell.

The rare-earth atoms, which are situated at three different Wyckoff positions, occupy one layer of the structure ($z = 0$) while the second one ($z = \frac{1}{2}$) is occupied by the palladium and indium atoms. Refined lattice parameters and atomic coordinates are presented in Table 1 and they are in good agreement with the previous results reported in Ref. [2] (see Fig. 2). Further details are given in Section 5. Fig. 2 presents dependences of the lattice parameters *a*, *b* and *c* and the unit cell volume *V* vs. effective ionic radius of rare-earths [13]. The dependences are almost linear and follow the lanthanide contraction.

Fig. 3 presents a projection of the unit cell of $Er_5Pd_2In_4$ onto the *ab*-plane and illustrates the coordination polyhedra of all the atoms, viz. [Er1In_8Er_4], [Er2$Pd_4In_6Er_6$], [Er3$Pd_2In_6Er_6$], [PdEr_6In_3], [In1-PdEr_8In_3] and [In2$Pd_2Er_8In_3$].

The distributions of Er atoms at different sites in $Er_5Pd_2In_4$ and atomic nets of erbium are shown in Fig. 4a. The shortest interatomic Er-Er (Fig. 4a) as well as Pd-In and In-In (Fig. 4b) distances in Å, according to refined crystallographic parameters (see Table 1), have been emphasized. It should be mentioned that in this two-layered structure the atoms of same sites are at the distance of the shortest unit cell parameter $c = 3.5971$ Å.

4. Magnetic properties

The results of dc magnetic measurements (RE = Tb–Tm) are presented in Fig. 5 while the ac data (RE = Tb–Er) in Fig. 6. The parameters characterizing the magnetic order, as determined from the above mentioned data, are listed in Table 2. A typical para- to ferro-/ferrimagnetic transition in $RE_5Pd_2In_4$ (RE = Tb–Er) manifests itself in presence of inflection point in the $\chi_{dc}(T)$ curve collected at 50 Oe. The transition is confirmed by maxima found in the $\chi_{ac}(T)$ data (H_{ac} = 2 Oe, H_{dc} = 0 Oe). The Curie temperatures range from about 16 K for RE = Er up to almost 100 K for RE = Tb. A number of additional anomalies in both the dc and ac magnetic susceptibility vs. temperature curves, identified either as maxima or extra inflection points, are found (see Table 2 for details). $Tm_5Pd_2In_4$ is an exception

Table 1
Crystallographic data obtained from Rietveld refinement of the X-ray powder diffraction patterns collected at room temperature for $RE_5Pd_2In_4$ (RE = Tb-Tm; $Lu_5Ni_2In_4$-type structure, space group *Pbam*, No. 55).

RE	Tb	Dy	Ho	Er	Tm
M [g/mol]	1466.74	1484.61	1496.76	1508.41	1516.78
a [Å]	18.1642(11)	18.0957(12)	18.0432(23)	17.9846(14)	17.9293(11)
b [Å]	8.0038(4)	7.9845(5)	7.9747(9)	7.9514(6)	7.9252(4)
c [Å]	3.6467(4)	3.6271(3)	3.6115(4)	3.5971(6)	3.5811(5)
V [Å^3]	530.17(7)	524.06(7)	519.65(11)	514.40(10)	508.85(8)
RE1 at 2a (0, 0, 0)					
RE2 at 4g (x, y, 0)	x = 0.2178(2)	0.2189(3)	0.2206(5)	0.2189(3)	0.2193(2)
	y = 0.2409(7)	0.2410(9)	0.2407(14)	0.2437(8)	0.2431(7)
RE3 at 4g (x, y, 0)	x = 0.4200(3)	0.4195(3)	0.4188(6)	0.4179(3)	0.4184(3)
	y = 0.1183(5)	0.1168(5)	0.1174(11)	0.1181(7)	0.1196(6)
Pd at 4h (x, y, $\frac{1}{2}$)	x = 0.3022(3)	0.3022(4)	0.3039(6)	0.3025(4)	0.3037(4)
	y = 0.0232(8)	0.0245(11)	0.0279(17)	0.0294(10)	0.0283(8)
In1 at 4h (x, y, $\frac{1}{2}$)	x = 0.5697(3)	0.5687(4)	0.5686(7)	0.5679(4)	0.5675(3)
	y = 0.2082(6)	0.2073(8)	0.2116(13)	0.2081(8)	0.2086(7)
In2 at 4h (x, y, $\frac{1}{2}$)	x = 0.8504(3)	0.8497(4)	0.8493(5)	0.8501(4)	0.8503(3)
	y = 0.0756(7)	0.0761(9)	0.0745(14)	0.0755(9)	0.0768(8)
B_{ov} [Å^2]	0.33(9)	0.14(9)	0.22(11)	0.56(10)	0.13(8)
R_f [%]	5.01	5.47	3.72	4.13	3.67
R_{Bragg} [%]	7.03	7.78	5.22	7.21	5.70

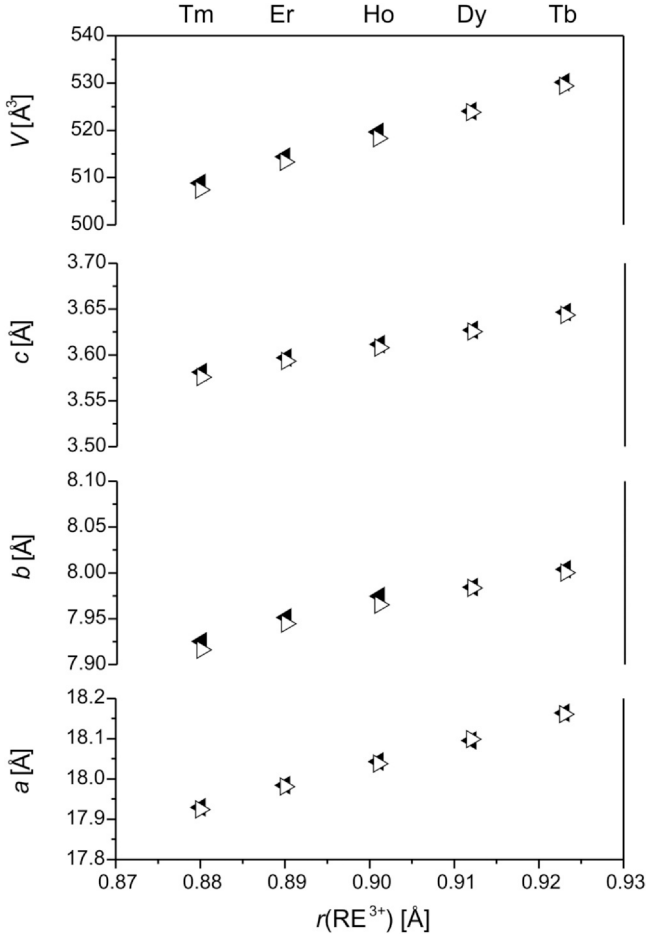

Fig. 2. Lattice parameters a, b and c along with the unit cell volume V as a function of r (RE^{3+}) – the effective ionic radii of rare-earths with coordination number VI. The radii were taken from [13]. The filled symbols refer to our experimental data while the open ones – to the literature data from Ref. [2].

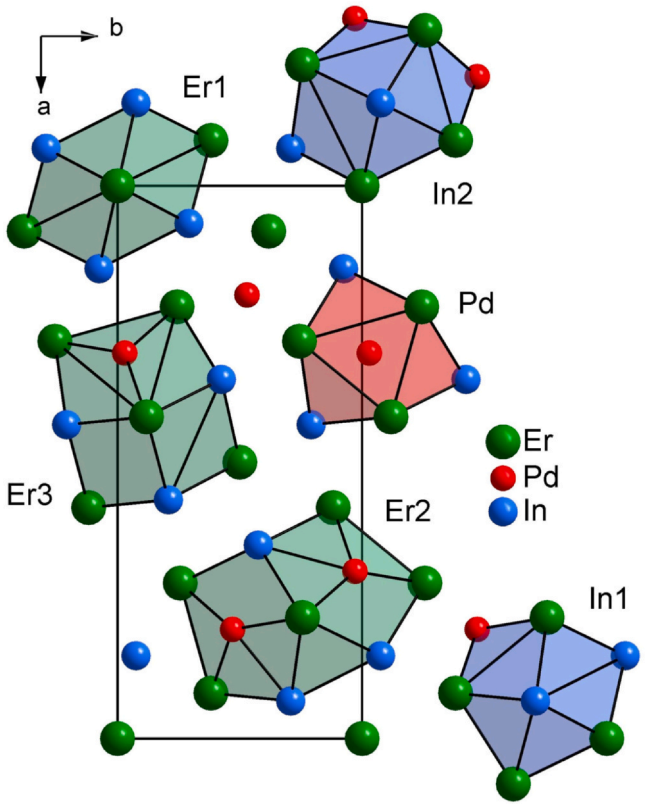

Fig. 3. Projection of the $Er_5Pd_2In_4$ crystal unit cell on the *ab*-plane together with coordination polyhedra of the atoms.

as its $\chi_{dc}(T)$ curve has at 4.3 K a maximum typical of para- to antiferromagnetic transition. For all investigated compounds a significant discrepancy between the ZFC and FC curves is noticeable below the respective critical temperature (Curie or Néel) of magnetic ordering.

Reciprocal magnetic susceptibility, collected at H = 1 kOe, becomes linear and therefore follows the Curie-Weiss law at high enough temperatures. The paramagnetic Curie temperatures are found positive for RE = Tb–Er or equal to zero in $Tm_5Pd_2In_4$. The effective magnetic moments per RE atoms are close to the values predicted for free RE^{3+} ions. The moments in the ordered state, as derived from

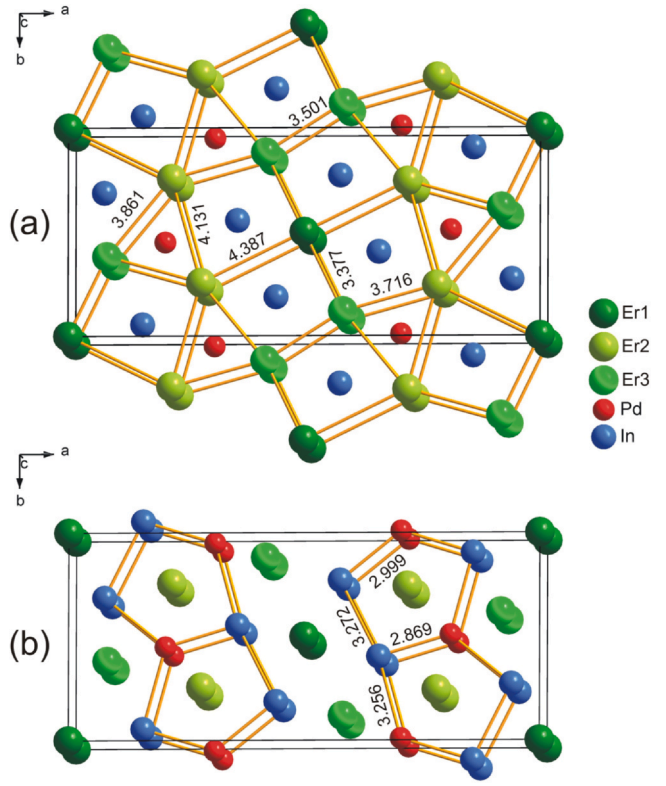

Fig. 4. Distribution of the Er atoms among different sites in $Er_5Pd_2In_4$. The shortest interatomic distances in Å, according to refined crystallographic parameters (see Table 1), have been emphasized: (a) Er-Er, (b) Pd-In and In-In.

magnetization measurements taken at $T = 2.0$ K and $H = 90$ kOe, are significantly smaller than those of free RE^{3+} ions.

The magnetization hysteresis loops have been recorded between $H = -90$ and 90 kOe at $T = 2.0$ K and selected higher temperatures. The primary curves taken at 2.0 K show metamagnetic transitions, characteristic of antiferromagnetic contribution to the magnetic structure, for RE = Tb, Dy and Tm. The hysteresis loops at the same temperature are characterized by coercivity fields which decrease with increasing number of the 4*f* electrons from 12.4 kOe for RE = Tb down to 0.10 kOe for RE = Tm.

5. Magnetic structures

The neutron powder diffraction data collected in the paramagnetic state confirm the crystal structure of the $Lu_5Ni_2In_4$-type (see Fig. 7a: diffraction pattern for $Tb_5Pd_2In_4$ taken at $T = 119.8$ K, which was chosen as a representative). Determined values of the lattice parameters *a*, *b* and *c* as well as the unit cell volume *V* are in good agreement with those determined from X-ray data at room temperature. At low temperatures additional peaks of magnetic origin are detected (Figs. 7b–d, 8a, 9a–b, 10a, 11a). According to the magnetic data (the values of effective magnetic moments are very close to those predicted for the RE^{3+} ions), the magnetism of $RE_5Pd_2In_4$ is related to the rare-earth atoms which occupy three Wyckoff sites:

2*a* sublattice: RE1_1 (0, 0, 0) and RE1_2 ($\frac{1}{2}$, $\frac{1}{2}$, 0).

4g1 sublattice: RE2_1 (x_{RE2}, y_{RE2}, 0), RE2_2 ($1 - x_{RE2}$, $1 - y_{RE2}$, 0), RE2_3 ($-x_{RE2} + \frac{1}{2}$, $y_{RE2} + \frac{1}{2}$, 0), and RE2_4 ($x_{RE2} + \frac{1}{2}$, $-y_{RE2} + \frac{1}{2}$, 0).

4g2 sublattice: RE3_1 (x_{RE3}, y_{RE3}, 0), RE3_2 ($1 - x_{RE3}$, $1 - y_{RE3}$, 0), RE3_3 ($-x_{RE3} + \frac{1}{2}$, $y_{RE3} + \frac{1}{2}$, 0), and RE3_4 ($x_{RE3} + \frac{1}{2}$, $-y_{RE3} + \frac{1}{2}$, 0).

The atomic positional parameters obtained from the refinements are listed in Table 1.

The possible magnetic structures can be determined using the formalism of the basis vectors (BV) of irreducible representations (IR), which depend on the crystal space group, magnetic propagation vector and the Wyckoff site of the magnetic atom. The representations allowed for each Wyckoff site occupied by RE atoms in $RE_5Pd_2In_4$ were calculated using BasIreps from the FullProf [11,12] package (the details of symmetry analysis can be found in the supplementary material). A Rietveld refinement of magnetic structures was performed for difference patterns, obtained by subtraction of pattern taken in the paramagnetic state from the patterns collected below the magnetic ordering temperature. The only exception is for $Dy_5Pd_2In_4$, where the magnetic structure was determined based on the full diffraction patterns due to high level of noise caused by a large absorption coefficient of Dy.

5.1. $Tb_5Pd_2In_4$

The above presented complex magnetic properties of $Tb_5Pd_2In_4$ are in agreement with thermal evolution of magnetic contribution to the powder neutron diffraction pattern (see Fig. 7b–7d). The Bragg reflections of magnetic origin at 69.8 K (see Fig. 7b) overlap with those of nuclear origin (compare with Fig. 7a) indicating a propagation vector $\vec{k}_1 = [0, 0, 0]$, i.e. the magnetic unit cell has the same size as the nuclear one. For the space group *Pbam* (No. 55), symmetry analysis gives four one-dimensional irreducible representations for the 2*a* site and eight one-dimensional irreducible representations for the 4*g*1 and 4*g*2 sites. Atoms occupying each particular sublattice belong to one orbit, which means that their magnetic moments are constrained by symmetry. The best agreement with the experimental data was obtained for magnetic structure model with magnetic moments in the 2*a* and 4*g*2 sites corresponding to the basis vectors of the IR3 representation (representation numbers follow the output files of BasIreps), which resulted in the ferromagnetic order along the *c*-axis, while the magnetic moments in the 4*g*1 sublattice remained disordered. The results of the Rietveld refinement are presented in Table 3, and the corresponding visualization of the magnetic structure at 69.8 K is shown in Fig. 7e. The magnetic moment at the 2*a* site is equal to 6.7(2) μ_B, and it is larger than 4.1(1) μ_B found at the 4*g*2 site.

The magnetic reflections at 39.7 K (Fig. 7c) are observed at different positions than those at higher temperature (Fig. 7b) indicating the existence of an additional magnetic phase transition between 40 and 70 K. The magnetic reflections at 39.7 K can be indexed with the propagation vector $\vec{k}_2 = [0, \frac{1}{2}, 0]$, which corresponds to an antiferromagnetic order with magnetic unit cell doubled along the *b*-axis when compared with the crystal unit cell. Symmetry analysis gives two representations for each sublattice, with magnetic moments ordered along the *c*-direction (IR1) or in the *ab*-plane (IR2). The agreement with the experimental pattern is obtained for magnetic moments in the 2a and 4g2 sites ordered antiferromagnetically along the *c*-axis (Fig. 7f, Table 4) while magnetic moments in the 4*g*1 site being still disordered. Symmetry allows for different values of magnetic moments for the Tb1_1 and Tb1_2 atoms (2*a* site), as well as for the pairs (Tb3_1, Tb3_2) and (Tb3_3, Tb3_4) in the 4*g*2 site. However, in order to obtain reasonable uncertainties, the magnetic moments on each sublattice were constrained to have equal absolute values. The obtained magnetic moments at 39.7 K are as follows: 7.4(3) μ_B for the 2*a* site and 7.0(2) μ_B for the 4*g*2 site.

The magnetic contribution to the pattern registered at 1.4 K consists of the reflections observed previously at 39.7 K ($\vec{k}_2 = [0, \frac{1}{2}, 0]$) plus additional group of reflections related to the

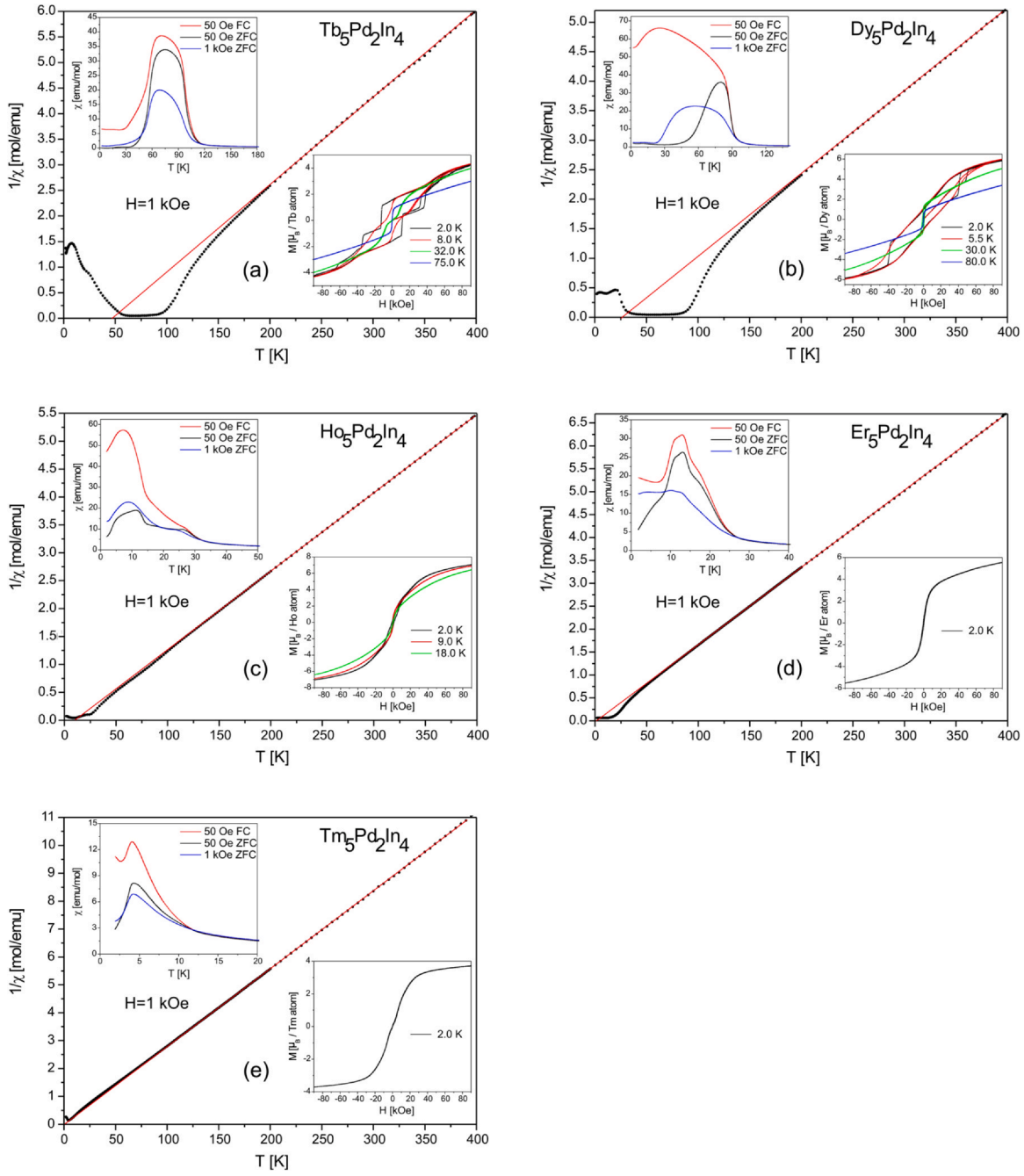

Fig. 5. Reciprocal magnetic susceptibility (circles) together with fitted line representing the Curie-Weiss law for $RE_5Pd_2In_4$: (a) RE = Tb, (b) Dy, (c) Ho, (d) Er and (e) Tm. The upper insets show the low temperature behavior measured at 50 Oe (ZFC and FC) and 1 kOe (ZFC). The lower insets show the isothermal magnetization vs. external magnetic field at selected temperatures.

propagation vector $\vec{k}_3 = [0, \frac{1}{2}, \frac{1}{2}]$ (see Fig. 7d). The latter vector corresponds to the magnetic unit cell doubled along both the *b*- and *c*-directions. The magnetic ordering at 1.4 K described by $\vec{k}_2 = [0, \frac{1}{2}, 0]$ is the same as that at 39.7 K, except larger values of magnetic moments equal to 8.0(4) μ_B and 8.3(3) μ_B for the 2*a* and 4g2 sublattices, respectively (Table 4). The basis vectors of irreducible representations obtained for $\vec{k}_3 = [0, \frac{1}{2}, \frac{1}{2}]$ are identical with those for $\vec{k}_2 = [0, \frac{1}{2}, 0]$, however, the Rietveld refinement proves that the $\vec{k}_3$ vector describes ordering in the *ab*-plane (Table 5). The main contribution to the antiferromagnetic structure related to $\vec{k}_3 = [0, \frac{1}{2}, \frac{1}{2}]$ comes from the 4g1 sublattice with magnetic moments of the Tb2_1 and Tb2_2 atoms equal to 7.0(1.5) μ_B and having similar components along the *a*- and *b*-directions while those of Tb2_3 and Tb2_4 being parallel to the *b*-axis and equal to 5.8(1.3) μ_B. The

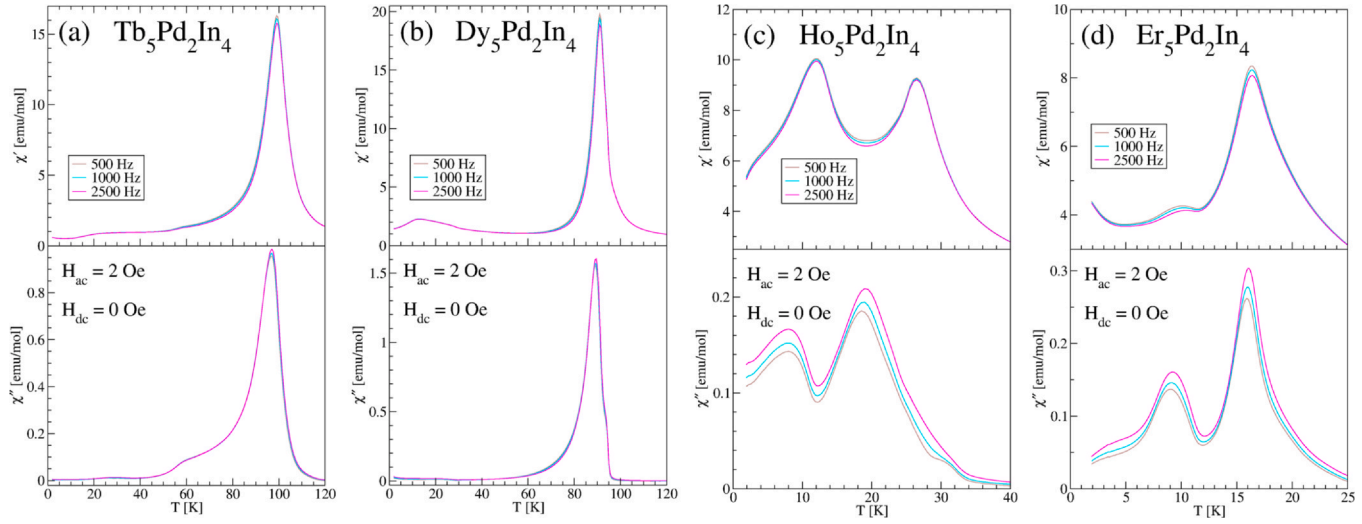

Fig. 6. ac magnetic susceptibility vs. temperature taken at selected frequencies between 500 Hz and 2500 Hz. χ' and χ'' refer to the real and imaginary components, respectively.

Table 2
Parameters characterizing magnetic order in $RE_5Pd_2In_4$ (RE = Tb–Tm) as derived from dc and/or ac magnetometric measurements. T_C and T_N denote the Curie and Néel temperatures, respectively. T_t refers to additional anomalies detected in the magnetic susceptibility vs. temperature curves. θ_p and μ_{eff} are the paramagnetic Curie temperature and effective magnetic moments obtained from reciprocal magnetic susceptibility. μ is the magnetic moment in the ordered state, measured at T = 2.0 K and H = 90 kOe. "exp." and "theor." denote the experimental and theoretical values, respectively. The critical fields (H_{cr}) indicating metamagnetic transitions have been determined from primary magnetization curves while the coercivity fields (H_{coer}) from hysteresis loops taken at selected temperatures.

RE	T_C [K]			T_N [K]	T_t [K]			θ_p [K]	$\mu_{eff}[\mu_B]$		$\mu[\mu_B]$		H_{cr} [kOe]	H_{coer} [kOe]
	χ_{dc}	χ'_{ac}	χ''_{ac}	χ_{dc}	χ_{dc}	χ'_{ac}	χ''_{ac}		exp.	theor.	exp.	theor.		
Tb	97^i	98^m	96.5^m		58^i, 75^m		60^m	+44	9.74	9.72	4.27	9.00	T = 2.0 K: 38, 66, 82	12.4
													T = 8.0 K: 24	7.8
													T = 32.0 K: 8.5	0.58
													T = 75.0 K:	0.044
Dy	88^i	89^m	89^m		24^{m,f}, 79^m	13.0^m		+26	10.68	10.63	5.90	10.00	T = 2.0 K: 50	9.9
													T = 5.5 K:	10.9
													T = 30.0 K:	1.0
													T = 80.0 K:	0.004
Ho	28.5^i	26.5^m			3.6^i, 11.2^m, 13.4^i	12.0^m	7.9^m, 18.5^m	+10.9	10.65	10.60	7.04	10.00	T = 2.0 K:	1.9
													T = 8.0 K:	0.3
													T = 18.0 K:	0.05
Er	16.5^i	16.3^m	15.8^m		10.0^i, 13.2^m 14.2^i, 20.5^i	10.0^m	8.7^m	+1.6	9.74	9.59	5.52	9.00	T = 2.0 K:	0.35
Tm				4.3^m				0.0	7.57	7.56	3.71	7.00	T = 2.0 K: 5.0	0.10

i – inflection point; m – maximum; f – determined from the FC curve

moments related to $\vec{k}_3$ in the remaining 2a and 4g2 sublattices have only the b-axis component equal to 3.6(1.4) μ_B for the 2a site, and 3.7(8) μ_B and 1.9(4) μ_B for the (Tb3_1, Tb3_2) and (Tb3_3, Tb3_4) pairs, respectively. The resultant magnetic structure at 1.4 K, described by the two propagation vectors $\vec{k}_2$ and $\vec{k}_3$, is presented in Fig. 7g.

5.2. $Dy_5Pd_2In_4$

Magnetic peaks in the patterns of $Dy_5Pd_2In_4$ are indexed by the $\vec{k}_1$ = [0, 0, 0] propagation vector. The magnetic structure at all studied temperatures below the Curie point is described by the basis vectors of the IR3 representation, indicating presence of the ferromagnetic order along the c-axis (Table 3). A representative diffraction pattern is shown in Fig. 8a. At 80.0, 65.0 and 40.0 K, the magnetic moments in the 4g1 site are found disordered while the moments in the 2a and 4g2 sites are parallel to each other. Therefore at these temperatures $Dy_5Pd_2In_4$ is a ferromagnet. The magnetic moments in 2a and 4g2 sites increase with decreasing temperature, reaching at 1.5 K the values 5.4(7) μ_B and 3.9(5) μ_B, respectively. The parallel orientation of magnetic moments in the 2a and 4g2 sublattices is preserved down to 1.5 K. Additionally, non-zero localized magnetic moments of 1.7(4) μ_B in the 4g1 sublattice, oriented in the opposite direction to the moments in the 2a and 4g2 sites, are derived from Rietveld refinement at 1.5 K. The resultant structure at 1.5 K is thus a ferrimagnetic one, as presented in Fig. 8b.

5.3. $Ho_5Pd_2In_4$

The magnetic peaks in the diffraction patterns of $Ho_5Pd_2In_4$ can be indexed using at least two different propagation vectors. Most of the reflections are indexed by $\vec{k}_1$ = [0, 0, 0] while two remaining satellites around the peak at 2θ = 7. 5° are indexed by $\vec{k}_4$ = [δ, 0, 0], implying an additional modulation of magnetic moments superimposed on the main structure (Fig. 9a–b). At 19.9 and 14.9 K, the experimental diffraction pattern (Fig. 9a) is reproduced assuming antiferromagnetic ordering in the 2a and 4g2 sublattices with magnetic moments being parallel to the c-axis according to the basis vectors of the IR1 representation of $\vec{k}_1$ = [0, 0, 0] (Table 3, Fig. 9c). The magnetic moments in the 4g1 sublattice remain disordered. At

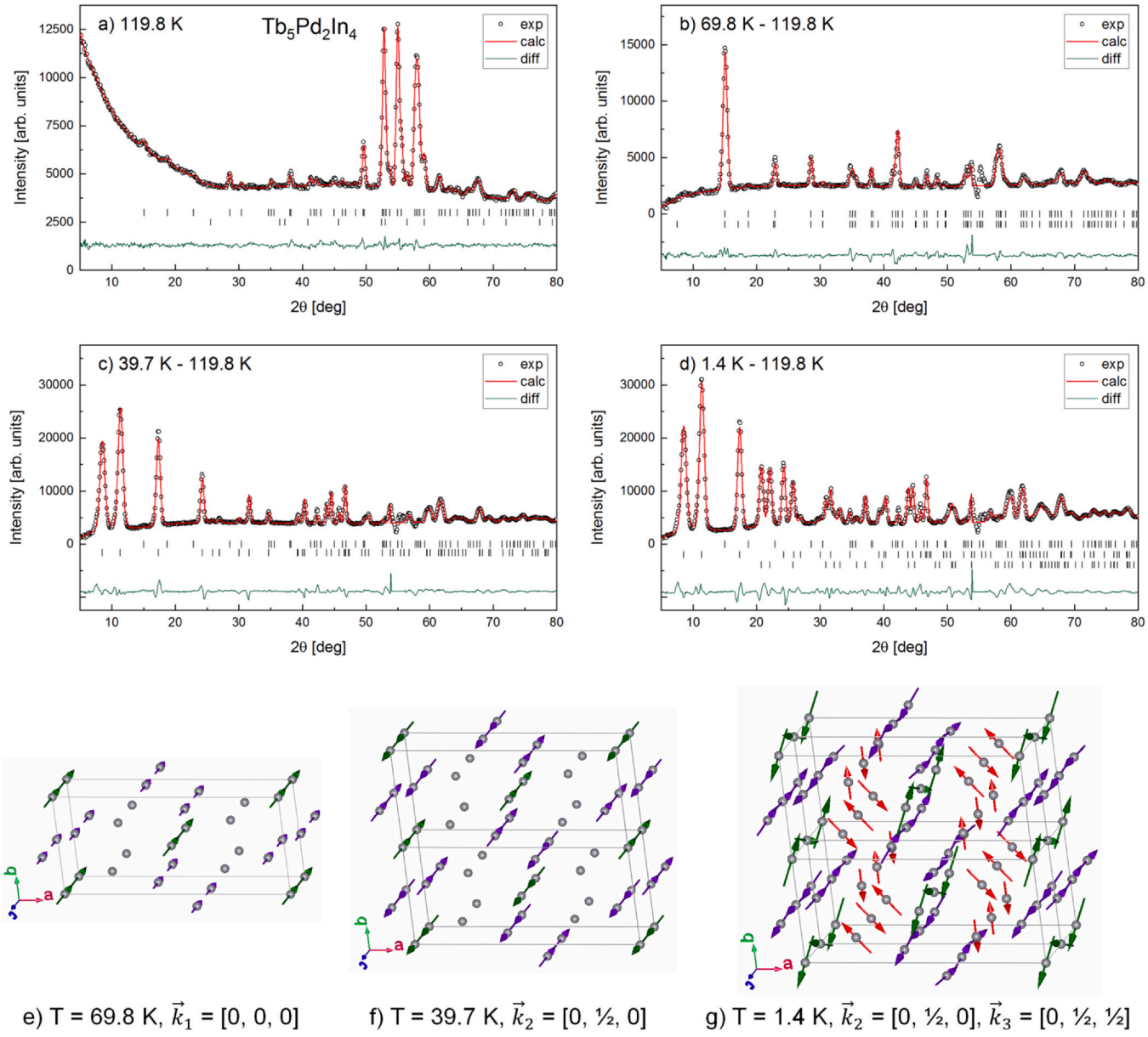

Fig. 7. Neutron powder diffraction patterns of $Tb_5Pd_2In_4$ (points) collected at (a) $T = 119.8$ K (paramagnetic state), (b) 69.8 K, (c) 39.7 K and (d) 1.4 K together with the results of Rietveld refinement (line) and difference curve (bottom line). The b-d insets are for difference patterns, obtained by subtracting the pattern collected at $T = 119.8$ K from the full diffraction patterns recorded at lower temperatures in order to obtain pure magnetic contribution. The $2\theta = 54 - 56^{\circ}$ range was excluded from refinement due to discrepancies in nuclear peak positions originating from thermal expansion of the unit cell. The first row of vertical bars indicates positions of the nuclear Bragg reflections. The second row refers to (a) small amount (3.0(3)% wt.) of the Tb_2Pd_2In impurity phase [14], (b) $\vec{k}_1 = [0, 0, 0]$ propagation vector and (c-d) $\vec{k}_2 = [0, \frac{1}{2}, 0]$. The third row in (d) corresponds to $\vec{k}_3 = [0, \frac{1}{2}, \frac{1}{2}]$. Magnetic unit cells in $Tb_5Pd_2In_4$ at (e) $T = 69.8$ K, (f) 39.7 K and (g) 1.4 K. The structure in (g) is a superposition of the structures described by two different propagation vectors ($\vec{k}_2 = [0, \frac{1}{2}, 0]$ and $\vec{k}_3 = [0, \frac{1}{2}, \frac{1}{2}]$). Magnetic moments in the 2*a*, 4*g*1 and 4*g*2 Wyckoff sites are denoted by the green, red and purple arrows, respectively (for the color figure, see the online version).

lower temperatures, 7.9 and 1.4 K, the diffraction peaks arising from the antiferromagnetic phase of $Ho_5Pd_2In_4$ mentioned above and denoted as phase I, are still present, but the refined magnetic moments are lower than those at 14.9 K. Therefore the phase I gradually disappears with decreasing temperature, which is confirmed by simultaneous appearance of new magnetic peaks (Fig. 9b). The new peaks can be also indexed by $\vec{k}_1 = [0, 0, 0]$, but they correspond to another magnetic phase, denoted as phase II, co-existing with phase I at lower temperatures. The magnetic moments in phase II are ordered according to combination of the basis vectors of BV1 of IR3 (ordering along the *c*-direction) and those of BV2 of IR5 (ordering along the *b*-direction). The resultant structure of phase II is ferrimagnetic: moments in the 2*a* and 4*g*2 sites are ordered ferromagnetically within the *bc*-plane, while the moments in the 4*g*1 site are oriented entirely along the *b*-axis, in almost opposite direction to the moments in the 2*a* and 4*g*2 sublattices (Fig. 9d).

Additional antiferromagnetic commensurate modulation ($\vec{k}_4 = [\frac{1}{4}, 0, 0]$) of magnetic moments in the 2*a* and 4*g*2 sublattices is

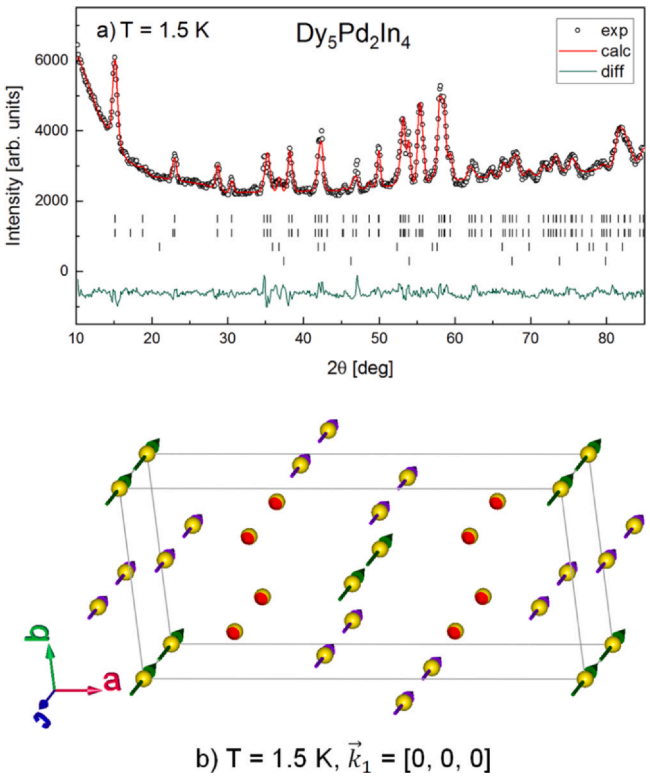

Fig. 8. (a) Neutron powder diffraction pattern of $Dy_5Pd_2In_4$ collected at $T = 1.5$ K together with the results of the Rietveld refinement (line) and difference curve (bottom line). The vertical bars indicate the positions of nuclear Bragg reflections (first row), magnetic peaks originating from the magnetic ordering described by $\vec{k}_1 = [0, 0, 0]$ (second row), and nuclear contributions from the $Dy_3Pd_2In_4$ (6.4(1.2)% wt.) [15] (third row) and Dy_2O_3 (1.9(4)% wt.) [16] (fourth row) impurity phases. (b) Magnetic unit cell in $Dy_5Pd_2In_4$ at $T = 1.5$ K.

detected at 19.9 and 14.9 K. The moments are parallel to the *c*-axis and correspond to the basis vectors of IR1 (Table 6). The magnetic moments in the 2*a* site (Ho1_1 and Ho1_2) are constrained by symmetry while the moments in the 4*g*2 site split into two orbits: the first one containing Ho3_1, Ho3_4 and the second one containing Ho3_2 and Ho3_3. As symmetry allows different magnitudes of magnetic moments in different orbits, the C_i coefficients for the first and second orbit were refined independently (see Table 6). Magnetic moments in the 2*a* site are found more than twice as large as those at each particular 4*g*2 orbit. The magnetic unit cell, with the size of four crystal unit cells quadrupled along the *a*-axis, is presented in Fig. 9e. At lower temperatures, where phase I is gradually disappearing, the satellites significantly broaden indicating a decrease in magnetic domain size. Due to small signal-to-background ratio for the satellites found in the patterns taken at 7.9 K and 1.4 K, the magnetic moments are determined with large uncertainties and therefore they are not listed in Table 6.

5.4. $Er_5Pd_2In_4$

Magnetic structure of $Er_5Pd_2In_4$ is again described by the propagation vector $\vec{k}_1 = [0, 0, 0]$ (Fig. 10b), but it corresponds to different set of basis vectors of irreducible representations than for the above reported magnetic structures in $RE_5Pd_2In_4$ (RE = Tb, Dy, Ho) (see Table 3). The magnetic moments in the 2*a* and 4*g*2 sublattices are ordered antiferromagnetically and are related to the basis vectors of IR7. For the 2*a* site, the contribution to the total magnetic moment along the *b*-axis is about twice as large as the contribution along the *a*-axis, while for the 4*g*2 site the whole contribution to the magnetic moment is solely along the *b*-axis. The magnetic moments in the 4*g*1 sublattice are disordered at 29.9 and 11.9 K, while at 7.9 K and 1.5 K they are ordered ferromagnetically along the *b*-axis, and they correspond to BV2 of IR5. Magnetic ordering at 7.9 K is presented in Fig. 10b.

5.5. $Tm_5Pd_2In_4$

The magnetic reflections observed for $Tm_5Pd_2In_4$ at 1.4 K (Fig. 11a) can be indexed by a set of two incommensurate propagation vectors: $\vec{k}_5 = [0.073(3), 0.451(1), \frac{1}{2}]$ and $\vec{k}_6 = [0, 0.335(2), \frac{1}{2}]$. Symmetry analysis performed for $\vec{k}_5 = [0.07, 0.45, \frac{1}{2}]$ has shown that all magnetic atoms are independent with respect to their magnitudes and orientations (symmetry does not impose any extra constrains) and two representations are possible: IR1 corresponding to magnetic ordering along the *c*-axis and IR2 corresponding to ordering within the *ab*-plane. Rietveld refinement for the $Tm_5Pd_2In_4$ data has shown that reasonable results are only possible for IR2. In order to reduce the number of fitting variables, the same amplitude of modulation of magnetic moment was assumed for all moments occupying the same Wyckoff site (see Table 7). Symmetry analysis performed for $\vec{k}_6 = [0, 0.34, \frac{1}{2}]$ results in four different representations. Rietveld refinement favors the magnetic structure related to the basis vectors of IR4 which involve magnetic moments within the *ab*-plane. The Tm1_1 and Tm1_2 atoms are constrained by symmetry, while each of the 4*g*1 and 4*g*2 sites split into two orbits: Tm2_1, Tm2_3 and Tm2_2, Tm2_4 (and the same for the Tm3 site). Again, the amplitude of modulation of magnetic moment has been constrained to be equal within each particular sublattice involving two orbits (Table 8). The refined magnetic structures are presented in Fig. 11b–c. For both propagation vectors, the ordering is antiferromagnetic and for each component of the magnetic structure the magnetic moments have similar absolute values for all sublattices. It is worth noting that the component magnetic structure in $Tm_5Pd_2In_4$, related to $\vec{k}_5 = [0.07, 0.45, \frac{1}{2}]$, resembles the magnetic structure in $Tb_5Pd_2In_4$ at 1.4 K, described by two propagation vectors $\vec{k}_2 = [0, \frac{1}{2}, 0]$ and $\vec{k}_3 = [0, \frac{1}{2}, \frac{1}{2}]$.

6. Discussion

The work reports the results of X-ray and neutron diffraction as well as dc and ac magnetic measurements for the $RE_5Pd_2In_4$ (RE = Tb-Tm) series of compounds. X-ray and neutron diffraction data confirm the orthorhombic crystal structure of the $Lu_5Ni_2In_4$-type. The crystal structure is a typical layered structure, where the layers are formed by the rare-earth atoms ($z = 0$) and they are separated by layers containing Pd and In atoms ($z = \frac{1}{2}$). The rare-earth atoms are located at three nonequivalent Wyckoff sites: the 2*a* site and two 4*g* sites with different atomic positional parameters.

Magnetic and neutron diffraction data indicate that the compounds have complex magnetic properties and the magnetic moments localized solely on the rare-earth atoms. The determined effective magnetic moment values in the paramagnetic state are close to those of the theoretical ones of the free RE^{3+} ions while the magnetic moments in the ordered state, as found from magnetization as well as from the neutron diffraction data, are smaller than those of free RE^{3+} ions. The latter discrepancy indicates a significant

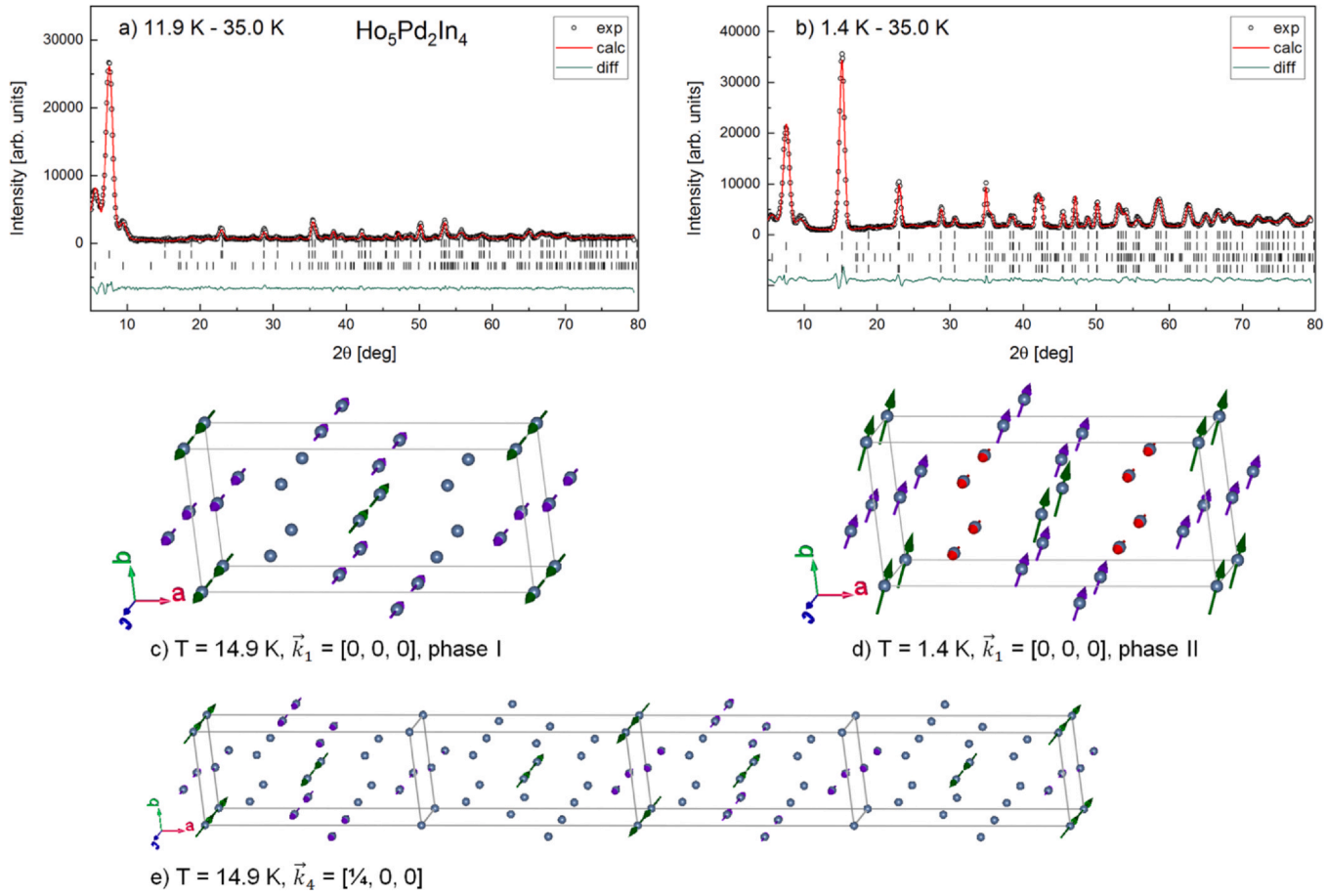

Fig. 9. Difference neutron powder diffraction patterns of $Ho_5Pd_2In_4$ (points) obtained by subtraction of the diffraction pattern collected at $T = 35.0$ K (paramagnetic phase) from those collected at (a) $T = 14.9$ K and (b) 1.4 K, together with the results of the Rietveld refinement (lines) and difference curves (bottom lines). The vertical bars indicate the positions of nuclear Bragg reflections (first row) and magnetic reflections from the antiferromagnetic magnetic phase I described by $\vec{k}_1 = [0, 0, 0]$ (second row), additional modulation related to $\vec{k}_4 = [\frac{1}{4}, 0, 0]$ (third row) and the ferrimagnetic phase II also described by $\vec{k}_1 = [0, 0, 0]$ (the fourth row in (b)). A weak reflection at $2\theta = 15.2^{\circ}$ originating from a small amount of the arising phase II is already noticeable in (a). Magnetic structures in $Ho_5Pd_2In_4$: (c) the phase I at $T = 14.9$ K and (d) the phase II at $T = 1.4$ K (both phases are described by the propagation vector $\vec{k}_1 = [0, 0, 0]$) and (e) the magnetic unit cell of a modulated structure at $T = 14.9$ K described by the additional propagation vector $\vec{k}_4 = [\frac{1}{4}, 0, 0]$.

influence of the Crystalline Electric Field (CEF) on the physical properties of $RE_5Pd_2In_4$. The positive values of the paramagnetic Curie temperatures, only with the exception for Tm where θ_p equals zero, indicate that ferromagnetic interactions are dominant. Fig. 12 shows the critical temperatures of magnetic ordering ($T_{C,N}$) together with paramagnetic Curie temperatures (θ_p) plotted against the de Gennes factor $(g_J - 1)^2 J(J + 1)$ for both the Ni- and Pd-based $RE_5T_2In_4$ (RE = Tb-Tm, T = Ni, Pd) systems. The observed deviations from linear dependence are another evidence of significant influence of the crystalline electric field (CEF) on stability of the magnetic order in both series of compounds [18]. Similar deviations, attributed to the influence of CEF, have been observed in $RERh_4B_4$ (RE - rare earth element) [19] and $RE_{11}T_4In_9$ (RE = Gd-Er; T = Ni, Pd) [20,21].

The low temperature experimental data presented in this work show that the $RE_5Pd_2In_4$ (RE = Tb-Tm) intermetallics undergo a number of temperature- and field-induced magnetic transitions. For the compounds with RE=Tb-Er some common features can be found, namely:

1. Below the Curie temperature a main contribution to the magnetic structure arises from a component of magnetic structure related to $\vec{k}_1 = [0, 0, 0]$ and formed by the localized rare-earth magnetic moments occupying the RE1 and RE3 sites. Further decrease of temperature leads to appearance of the magnetic ordering at the RE2 site. Additional antiferromagnetic components of magnetic structures with enlarged magnetic unit cell are observed in $Tb_5Pd_2In_4$ ($\vec{k}_2 = [0, \frac{1}{2}, 0]$ and $\vec{k}_3 = [0, \frac{1}{2}, \frac{1}{2}]$) and $Ho_5Pd_2In_4$ ($\vec{k}_4 = [\frac{1}{4}, 0, 0]$).
2. The direction of magnetic moments is strictly correlated with the electronic properties of the rare-earth elements, indicating especially a strong influence of the crystalline electric field (CEF). Namely, just below the Curie point the magnetic moments of

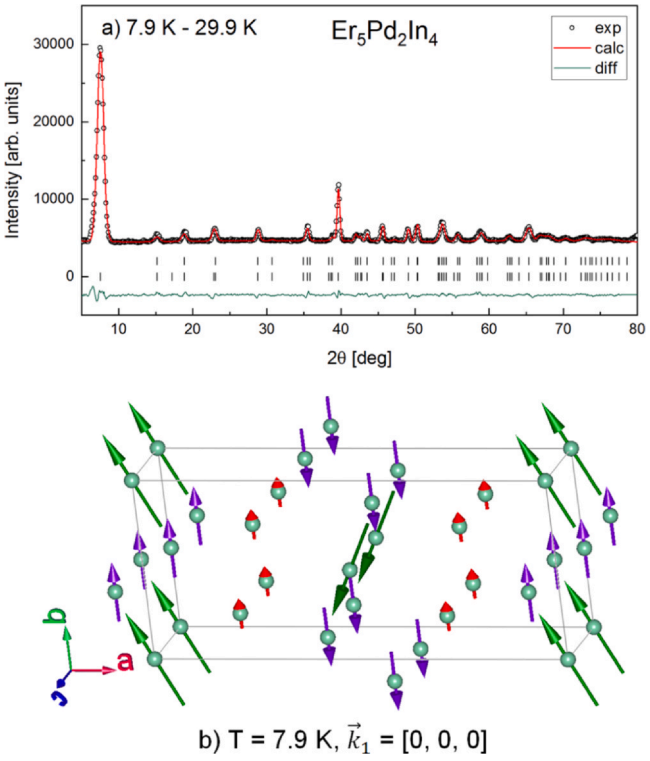

Fig. 10. (a) Difference neutron powder diffraction pattern of $Er_5Pd_2In_4$ (points) obtained by subtraction of the diffraction pattern collected at T = 29.9 K (paramagnetic phase) from that collected at T = 7.9 K, together with the results of the Rietveld refinement (line) and difference curve (bottom line). The vertical bars indicate the positions of nuclear Bragg reflections (first row) and magnetic reflections originating from the magnetic ordering described by $\vec{k}_1$ = [0, 0, 0] (second row). (b) Magnetic unit cell in $Er_5Pd_2In_4$ at T = 7.9 K.

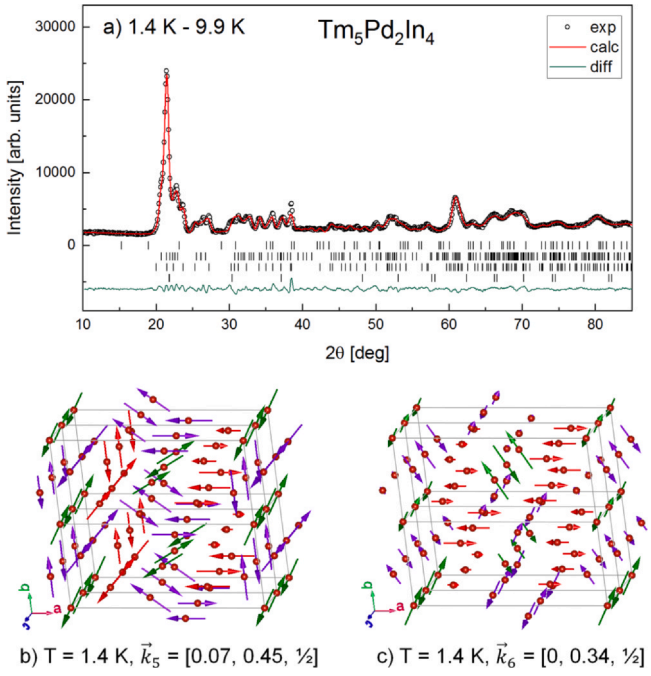

Fig. 11. (a) Difference neutron powder diffraction pattern of $Tm_5Pd_2In_4$ (points) obtained by subtraction of the diffraction pattern collected at T = 9.9 K (paramagnetic phase) from that collected at T = 1.4 K, together with the results of the Rietveld refinement (line) and difference curve (bottom line). The vertical bars indicate the positions of nuclear Bragg reflections (first row) and magnetic peaks originating from the magnetic ordering described by $\vec{k}_5$ = [0.073(3), 0.451(1), $\frac{1}{2}$] (second row) and $\vec{k}_6$ = [0, 0.335(2), $\frac{1}{2}$] (third row) as well as magnetic peaks from the TmPdIn impurity phase [17] (fourth row). Modulated magnetic structures in $Tm_5Pd_2In_4$ at T = 1.4 K described by the propagation vectors (b) $\vec{k}_5$ = [0.073(3), 0.451(1), $\frac{1}{2}$] and (c) $\vec{k}_6$ = [0, 0.335(2), $\frac{1}{2}$]. The magnetic unit cell is not defined due to incommensurability of the propagation vectors, therefore representative fragments of each structure are shown instead.

RE = Tb, Dy and Ho are parallel to the *c*-axis while those of RE = Er lie in the *ab*-plane. Such a behavior is commonly found in rare-earth intermetallics and it is related to the sign of the Stevens operator α_J which is negative for Tb, Dy and Ho but positive for Er [22]. Interestingly, the magnetic moments in $RE_5Pd_2In_4$ (RE = Tb-Tm) undergo a reorientation with decreasing temperature and at low temperatures they are aligned within the *ab*-plane for Tb and Er or within the *bc*-plane for Ho, while they are parallel to the *c*-axis for Dy.

3. Similarities between magnetic structures in the isostructural $RE_5Ni_2In_4$ compounds are noticeable. The magnetic structures have already been reported for the Tb-, Ho- [4] and Er-based compounds [8]. A ferro-/ferrimagnetic order, related to $\vec{k}$ = [0, 0, 0] and formed by the magnetic moments at the RE1 and RE3 sites, develops in $Tb_5Ni_2In_4$ below T_C = 125 K. Additional incommensurate antiferromagnetic cycloidal component appears below T_N = 20 K in the RE2 sublattice ($\vec{k}$ = [0, 0.636, $\frac{1}{2}$]). In $Ho_5Ni_2In_4$ the RE1 and RE3 moments form below T_N = 31 K a commensurate antiferromagnetic structure described by the propagation vector $\vec{k}$ = [0, 0, 0]. The structure transforms at 25 K into ferro-/ferrimagnetic one involving a magnetic order of holmium in all three sublattices. The magnetic ordering scheme in $Er_5Ni_2In_4$ is slightly different as a non-collinear ferro-/ferrimagnetism ($\vec{k}$ = [0, 0, 0]), involving both 4*g* sites (RE2 and RE3 sublattices) develops below T_C = 18.5 K while the 2*a* (RE1) site shows an antiferromagnetic ordering ($\vec{k}$ = [0, 0, $\frac{1}{2}$]) below about 2 K.

In the investigated compounds the rare-earth magnetic moments occupying different sublattices order at different temperatures. This behavior is strongly correlated with the distribution of the rare-earth atoms in the crystal unit cell. The framework of the crystal structure in $RE_5Pd_2In_4$ is determined by the shortest Pd-In and In-In bonds. These elements form the chains of distorted pentagonal prisms [$REPd_4In_6$] running along the *b*-axis (see Fig. 4b). The RE2 moments are situated in the center of the polyhedron, while the RE1 and RE3 ones are positioned between the chains. In the investigated compounds a clear hierarchy of ordering temperatures related to different rare-earth sublattices is observed. In most cases the moments in the RE1 and RE3 sites order at higher temperatures than those in the RE2 site. It is worth noting that the shortest rare-earth interatomic distances are those between the RE1-RE3 atoms (~3.4 Å) and

Table 3
Component of the magnetic structures in $RE_5Pd_2In_4$ (RE = Tb-Er) described by the propagation vector $\vec{k}_1 = [0, 0, 0]$. IR denote irreducible representations while BV are their basis vectors obtained by symmetry analysis for the 2*a* and 4*g* (identical for 4*g*1 and 4*g*2) Wyckoff sites of *Pbam* space group. The total number of possible IR for the 4*g* site equals eight but for better clarity those not used in the refinement are omitted. C_i coefficients denote the contribution along each BV to the total magnetic moment of an atom.

		IR1	IR3	IR5		IR7			
	$\vec{k}_1 = [0,0,0]$	BV1	BV1	BV1	BV2	BV1	BV2		
2*a*	RE1_1 (0, 0, 0)	0 0 1	0 0 1	1 0 0	0 1 0	1 0 0	0 1 0		
	RE1_2 ($\frac{1}{2}$, $\frac{1}{2}$, 0)	0 0 −1	0 0 1	−1 0 0	0 1 0	1 0 0	0 −1 0		
4*g*	RE2,3_1 (x, y, 0)	0 0 1	0 0 1	1 0 0	0 1 0	1 0 0	0 1 0		
	RE2,3_2 ($1-x$, $1-y$, 0)	0 0 1	0 0 1	1 0 0	0 1 0	1 0 0	0 1 0		
	RE2,3_3 ($-x+\frac{1}{2}$, $y+\frac{1}{2}$, 0)	0 0 −1	0 0 1	−1 0 0	0 1 0	1 0 0	0 −1 0		
	RE2,3_4 ($x+\frac{1}{2}$, $-y+\frac{1}{2}$, 0)	0 0 −1	0 0 1	−1 0 0	0 1 0	1 0 0	0 −1 0		
T [K]		C_1 [μ_B]	C_1 [μ_B]	C_1 [μ_B]	C_2 [μ_B]	C_1 [μ_B]	C_2 [μ_B]	μ_{tot} [μ_B]	R_{mag} [%]
	$Tb_5Pd_2In_4$								
69.8	Tb1 (2*a*)		6.7(2)					6.7(2)	11.8
	Tb3 (4*g*2)		4.1(1)					4.1(1)	
	$Dy_5Pd_2Ni_4$								
80.0	Dy1 (2*a*)		3.4(5)					3.4(5)	13.0
	Dy3 (4*g*2)		1.4(4)					1.4(4)	
65.0	Dy1 (2*a*)		4.2(4)					4.2(4)	11.2
	Dy3 (4*g*2)		2.0(4)					2.0(4)	
40.0	Dy1 (2*a*)		4.7(4)					4.7(4)	7.65
	Dy3 (4*g*2)		2.8(3)					2.8(3)	
1.5	Dy1 (2*a*)		5.4(7)					5.4(7)	9.19
	Dy2 (4*g*1)		−1.7(4)					1.7(4)	
	Dy3 (4*g*2)		3.9(5)					3.9(5)	
	$Ho_5Pd_2In_4$								
19.9	Ho1 (2*a*)	4.8(1)						4.8(1)	3.28
	Ho3 (4*g*2)	−3.1(1)						3.1(1)	
14.9	Ho1 (2*a*)	5.3(2)						5.3(2)	2.83
	Ho3 (4*g*2)	−3.7(1)						3.7(1)	
7.9	Ho1 (2*a*)	4.3(3)	−5.4(3)		3.6(5)			I) 4.3(3)	I) 2.68
								II) 6.4(5)	II) 3.70
	Ho2 (4*g*1)		2.7(1.0)					II) 2.7(1.0)	
	Ho3 (4*g*2)	−2.4(2)	−4.0(2)		1.7(4)			I) 2.4(2)	
								II) 4.3(3)	
1.4	Ho1 (2*a*)	4.6(3)	−5.3(3)		3.6(5)			I) 4.6(3)	I) 3.10
								II) 6.4(5)	II) 4.49
	Ho2 (4*g*1)		5.1(2)					II) 5.1(2)	
	Ho3 (4*g*2)	−2.3(2)	−4.4(2)		1.7(4)			I) 2.3(2)	
								II) 4.7(3)	
	$Er_5Pd_2In_4$								
14.9	Er1 (2*a*)					−1.4(2)	3.9(1)	4.1(2)	8.04
	Er3 (4*g*2)						−1.8(1)	1.8(1)	
11.9	Er1 (2*a*)					−2.5(2)	5.9(2)	6.5(2)	4.44
	Er3 (4*g*2)						−3.1(1)	3.1(1)	
7.9	Er1 (2*a*)					−3.4(3)	6.8(2)	7.6(3)	6.28
	Er2 (4*g*1)				2.2(2)			2.2(2)	
	Er3 (4*g*2)						−4.3(1)	4.3(1)	
1.4	Er1 (2*a*)					−3.9(4)	6.9(3)	7.9(5)	6.68
	Er2 (4*g*1)				2.7(3)			2.7(3)	
	Er3 (4*g*2)						−6.0(2)	6.0(2)	

Table 4
Component of the magnetic structure in $Tb_5Pd_2In_4$ described by the IR1 representation obtained by symmetry analysis for the 2*a* and 4g2 Wyckoff sites of the *Pbam* space group for the propagation vector $\vec{k}_2 = [0, \frac{1}{2}, 0]$. C_i coefficients denote the contribution along each basis vector (BV) to the total magnetic moment, $\Delta\phi$ is the magnetic phase factor calculated with respect to Tb1_1.

		IR1						
	$\vec{k}_2 = [0, \frac{1}{2}, 0]$	BV1	BV2	BV3	BV4			
2*a*	RE1_1 (0, 0, 0)	0 0 1	-	0 0 0	-			
	RE1_2 ($\frac{1}{2}$, $\frac{1}{2}$, 0)	0 0 0	-	0 0 −1	-			
4*g*	RE3_1 (x, y, 0)	0 0 1	0 0 0	0 0 0	0 0 1			
	RE3_2 ($1-x$, $1-y$, 0)	0 0 −1	0 0 0	0 0 0	0 0 1			
	RE3_3 ($-x+\frac{1}{2}$, $y+\frac{1}{2}$, 0)	0 0 0	0 0 1	0 0 −1	0 0 0			
	RE3_4 ($x+\frac{1}{2}$, $-y+\frac{1}{2}$, 0)	0 0 0	0 0 −1	0 0 −1	0 0 0			
T [K]	$Tb_5Pd_2In_4$	C_1 [μ_B]	C_2 [μ_B]	C_3 [μ_B]	C_4 [μ_B]	$\Delta\phi$ [$\frac{1}{2\pi}$]	μ_{tot} [μ_B]	R_{mag} [%]
39.7	Tb1_1 (2*a*)	7.4(3)		−7.4(3)		0	7.4(3)	6.76
	Tb3_1 (4*g*2)		−7.0(2)		7.0(2)	−0.018(4)	7.0(2)	
1.4	Tb1_1 (2*a*)	8.0(4)		−8.0(4)		0	8.0(4)	5.35
	Tb3_1 (4*g*2)		−8.3(3)		8.3(3)	−0.011(6)	8.3(3)	

Table 5
Component of the magnetic structure in $Tb_5Pd_2In_4$ at 1.4 K described by the IR2 representation obtained by symmetry analysis for the 2*a* and 4*g* (identical for 4*g*1 and 4*g*2) Wyckoff sites of the *Pbam* space group for the propagation vector $\vec{k}_3 = [0, \frac{1}{2}, \frac{1}{2}]$. C_i coefficients (given in μ_B) denote the contribution along each basis vector (BV) to the total magnetic moment, $\Delta\phi$ is the magnetic phase factor calculated with respect to Tb1_1.

		IR2										
	$\vec{k}_3 = [0, \frac{1}{2}, \frac{1}{2}]$	BV1	BV2	BV3	BV4	BV5	BV6	BV7	BV8			
2*a*	RE1_1 (0, 0, 0)	-	-	0 0 0	0 0 0	-	-	1 0 0	0 1 0			
	RE1_2 ($\frac{1}{2}, \frac{1}{2}$, 0)	-	-	1 0 0	0 −1 0	-	-	0 0 0	0 0 0			
4*g*	RE2,3_1 (*x*, *y*, 0)	1 0 0	0 1 0	0 0 0	0 0 0	0 0 0	0 0 0	1 0 0	0 1 0			
	RE2,3_2 (1 − *x*, 1 − *y*, 0)	1 0 0	0 1 0	0 0 0	0 0 0	0 0 0	0 0 0	−1 0 0	0 −1 0			
	RE2,3_3 ($-x + \frac{1}{2}, y + \frac{1}{2}$, 0)	0 0 0	0 0 0	1 0 0	0 −1 0	−1 0 0	0 1 0	0 0 0	0 0 0			
	RE2,3_4 ($x + \frac{1}{2}, -y + \frac{1}{2}$, 0)	0 0 0	0 0 0	1 0 0	0 −1 0	1 0 0	0 −1 0	0 0 0	0 0 0			
T [K]	$Tb_5Pd_2In_4$	C_1 [μ_B]	C_2 [μ_B]	C_3 [μ_B]	C_4 [μ_B]	C_5 [μ_B]	C_6 [μ_B]	C_7 [μ_B]	C_8 [μ_B]	$\Delta\phi$ [$\frac{1}{2\pi}$]	μ_{tot} [μ_B]	R_{mag} [%]
1.4	Tb1_1 (2*a*)				−3.6(1.4)				3.6(1.4)	0	3.6(1.4)	7.42
	Tb2_1, Tb2_2 (4*g*1)							−4.5(1.0)	5.4(1.6)	0.62(5)	7.0(1.5)	
	Tb2_3, Tb2_4 (4*g*1)				5.8(1.3)						5.8(1.3)	
	Tb3_1, Tb3_2 (4*g*2)								3.7(8)	0.79(4)	3.7(8)	
	Tb3_3, Tb3_4 (4*g*2)				−1.9(1.4)						1.9(1.4)	

Table 6
Component of the magnetic structure in $Ho_5Pd_2In_4$ described by the IR1 representation obtained by symmetry analysis for the 2*a* and 4*g*2 Wyckoff sites of the *Pbam* space group for the propagation vector $\vec{k}_4 = [\frac{1}{4}, 0, 0]$. C_i coefficients denote the contribution along each basis vector (BV) to the total magnetic moment, $\alpha = |\cos(\delta\pi)|$, $\beta = |\sin(\delta\pi)|$ where $\delta = ¼$.

		IR1		
	$\vec{k}_4 = [\frac{1}{4}, 0, 0]$	BV1		
2*a*	RE1_1 (0, 0, 0)	0 0 1		
	RE1_2 ($\frac{1}{2}, \frac{1}{2}$, 0)	0 0 ($-\alpha + i\beta$)		
4*g*	RE3_1 (*x*, *y*, 0)	0 0 1		
	RE3_2 (1 − *x*, 1 − *y*, 0)	0 0 1		
	RE3_3 ($-x + \frac{1}{2}, y + \frac{1}{2}$, 0)	0 0 ($-\alpha - i\beta$)		
	RE3_4 ($x + \frac{1}{2}, -y + \frac{1}{2}$, 0)	0 0 ($-\alpha + i\beta$)		
T [K]	$Ho_5Pd_2In_4$	C_1 [μ_B]	μ_{tot} [μ_B]	R_{mag} [%]
19.9	Ho1 (2*a*)	7.4(6)	7.4(6)	9.91
	Ho3_1, Ho3_4 (4*g*2)	−2.6(4)	2.6(4)	
	Ho3_2, Ho3_3 (4*g*2)	−2.4(3)	2.4(3)	
14.9	Ho1 (2*a*)	8.1(9)	8.1(9)	9.63
	Ho3_1, Ho3_4 (4*g*2)	−3.9(5)	3.9(5)	
	Ho3_2, Ho3_3 (4*g*2)	−2.5(4)	2.5(4)	

the RE3-RE3 ones (~3.5 Å) within the *ab*-plane (see Fig. 4). Both these distances are smaller than the sum of atomic radii equal to about 3.55 Å. Such a result suggests that the exchange interactions within the *ab*-plane involving the RE1 and RE3 atoms are mostly driven by the Campbell model-type mechanism [23]. The model assumes local interaction between the *f*- and *d*-orbitals (within individual rare-earth atom) and subsequently the direct exchange interactions between different atoms via the *d*-*d* orbitals. The interactions have local character as they are limited by the sum of radii of the atoms involved. The RE2 sublattice is more separated as the shortest RE1-RE2, RE2-RE2 and RE2-RE3 distances equal about 4.4, 3.6 and 3.7 Å, respectively. Such large interatomic distances exclude any direct interactions and suggest indirect exchange interactions via conduction electrons of the RKKY-type [24]. These interactions have more long-range character than those predicted by the Campbell model and therefore the RKKY-type interactions support appearance with decreasing temperature of the antiferromagnetic phases related to $\vec{k}_2 = [0, \frac{1}{2}, 0]$, $\vec{k}_3 = [0, \frac{1}{2}, \frac{1}{2}]$) (RE = Tb) or $\vec{k}_4 = [\frac{1}{4}, 0, 0]$ (RE = Ho).

Table 7
Component of the magnetic structure in $Tm_5Pd_2In_4$ at 1.4 K described by the IR2 representation obtained by symmetry analysis for the 2*a* and 4*g* (identical for 4*g*1 and 4*g*2) Wyckoff sites of the *Pbam* space group for the propagation vector $\vec{k}_5 = [0.073(3), 0.451(1), \frac{1}{2}]$. C_i coefficients denote the contribution along each basis vector (BV) to the total magnetic moment, while $\Delta\phi$ is the magnetic phase factor calculated with respect to Tm1_1.

		IR2				
	$\vec{k}_5 = [0.07, 0.45, \frac{1}{2}]$	BV1	BV2			
2*a*	RE1_1 (0, 0, 0)	1 0 0	0 1 0			
	RE1_2 ($\frac{1}{2}, \frac{1}{2}$, 0)	1 0 0	0 1 0			
4*g*	RE2,3_1 (*x*, *y*, 0)	1 0 0	0 1 0			
	RE2,3_2 (1 − *x*, 1 − *y*, 0)	1 0 0	0 1 0			
	RE2,3_3 ($-x + \frac{1}{2}, y + \frac{1}{2}$, 0)	1 0 0	0 1 0			
	RE2,3_4 ($x + \frac{1}{2}, -y + \frac{1}{2}$, 0)	1 0 0	0 1 0			
T [K]	$Tm_5Pd_2In_4$	C_1 [μ_B]	C_2 [μ_B]	$\Delta\phi$ [$\frac{1}{2\pi}$]	μ_{tot} [μ_B]	R_{mag} [%]
1.4	Tm1_1 (2*a*)	3.8(3)	6.6(5)	0	7.6(6)	4.94
	Tm1_2 (2*a*)	6.6(5)	3.8(3)	0	7.6(6)	
	Tm2_1 (4*g*1)	4.7(8)	5.1(8)	0	7.0(4)	
	Tm2_2 (4*g*1)	−7.0(4)		0.21(3)	7.0(4)	
	Tm2_3 (4*g*1)		7.0(4)	−0.40(3)	7.0(4)	
	Tm2_4 (4*g*1)	7.0(4)		0	7.0(4)	
	Tm3_1 (4*g*2)	5.8(5)	−4.5(6)	0	7.3(3)	
	Tm3_2 (4*g*2)	-7.3(3)		0.05(3)	7.3(3)	
	Tm3_3 (4*g*2)	−5.0(9)	−5.4(9)	0	7.3(3)	
	Tm3_4 (4*g*2)		−7.3(3)	0	7.3(3)	

Table 8
Component of the magnetic structure in $Tm_5Pd_2In_4$ at 1.4 K described by the IR4 representation obtained by symmetry analysis for the 2*a* and 4*g* (identical for 4*g*1 and 4*g*2) Wyckoff sites of the *Pbam* space group for the propagation vector $\vec{k}_6 = [0, 0.335(2), \frac{1}{2}]$. C_i coefficients denote the contribution along each basis vector (BV) to the total magnetic moment, $\Delta\phi$ is the magnetic phase factor calculated with respect to Tm1_1, $\alpha = |\cos(\delta\pi)|$, $\beta = |\sin(\delta\pi)|$ where $\delta = 0.335(2)$.

		IR4				
	$\vec{k}_6 = [0, 0.34, \frac{1}{2}]$	BV1	BV2			
2*a*	RE1_1 (0, 0, 0)	1 0 0	0 1 0			
	RE1_2 ($\frac{1}{2}$, $\frac{1}{2}$, 0)	$(\alpha - i\beta)$ 0 0	0 $(-\alpha + i\beta)$ 0			
4*g*	RE2,3_1 (x, y, 0)	1 0 0	0 1 0			
	RE2,3_2 ($1 - x$, $1 - y$, 0)	1 0 0	0 1 0			
	RE2,3_3 ($-x + \frac{1}{2}$, $y + \frac{1}{2}$, 0)	$(\alpha - i\beta)$ 0 0	0 $(-\alpha + i\beta)$ 0			
	RE2,3_4 ($x + \frac{1}{2}$, $-y + \frac{1}{2}$, 0)	$(\alpha + i\beta)$ 0 0	0 $(-\alpha - i\beta)$ 0			
T [K]	$Tm_5Pd_2In_4$	C_1 [μ_B]	C_2 [μ_B]	$\Delta\phi$ [$\frac{1}{2\pi}$]	μ_{tot} [μ_B]	R_{mag} [%]
1.4	Tm1_1 (2*a*)	−3.4(7)	−6.0(6)	0	6.9(9)	6.83
	Tm2_1, Tm2_3 (4*g*1)	5.3(6)		0.30(5)	5.3(6)	
	Tm2_2, Tm2_4 (4*g*1)	5.3(6)		0.13(7)	5.3(6)	
	Tm3_1, Tm3_3 (4*g*2)	2.6(7)	4.4(5)	0	5.1(8)	
	Tm3_2, Tm3_4 (4*g*2)	2.6(7)	4.4(5)	0.37(6)	5.1(8)	

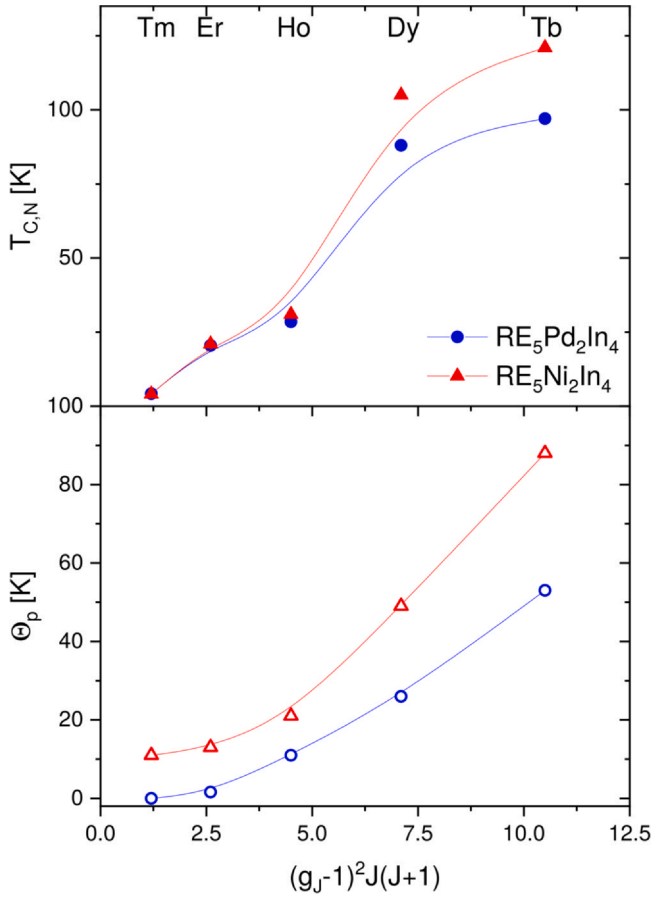

Fig. 12. Critical temperatures of magnetic ordering ($T_{C,N}$) together with paramagnetic Curie temperatures (θ_p) vs. de Gennes factor for $RE_5T_2In_4$ (RE = Tb-Tm, T = Ni, Pd). The data for T = Ni have been taken from Refs. [5-10] while those for T = Pd are reported in this work.

7. Conclusions

The $RE_5Pd_2In_4$ compounds (RE = Tb-Tm) with complex crystal structure in which the rare-earth atoms occupy three nonequivalent sites, present interesting magnetic properties including complex magnetic structures formed by the magnetic moments localized on the rare-earth atoms. Magnetic moments at different sublattices (Wyckoff sites) have different magnitudes and order at different temperatures. Just below the critical temperature a magnetic ordering described by $\vec{k}_1 = [0, 0, 0]$ is observed. For RE = Tb and Ho an antiferromagnetic component of the magnetic structure with enlarged magnetic unit cell develops. $Tm_5Pd_2In_4$ is an exception as its magnetic structure is purely antiferromagnetic and incommensurate within the whole temperature range below the critical temperature. Observed magnetic structures result from complex magnetic interactions involving the direct local exchange interactions related to the Campbell model and the indirect long-range ones of the RKKY-type. An influence of the crystalline electric field (CEF) on the direction of magnetic moments is noticeable.

CRediT authorship contribution statement

Stanisław Baran: Investigation, Writing - original draft, Writing - review & editing, Supervision. **Aleksandra Deptuch:** Formal analysis, Writing - original draft, Visualization. **Manfred Reehuis:** Investigation. **Yuriy Tyvanchuk:** Formal analysis, Investigation, Writing - original draft, Visualization. **Fabiano Yokaichiya:** Investigation. **Andrzej Szytuła:** Investigation, Writing - original draft, Writing - review & editing, Supervision.

Declaration of Competing Interest

The authors declare that they have no known competing financial interests or personal relationships that could have appeared to influence the work reported in this paper.

Acknowledgements

The research was partially carried out with the equipment purchased thanks to the financial support of the European Regional Development Fund in the framework of the Polish Innovation Economy Operational Program (contract no. POIG.02.01.00-12-023/08).

Kind hospitality and financial support extended to two of us (S. B. and A. S.) by the Helmholtz-Zentrum Berlin für Materialien und Energie (HZB) is gratefully acknowledged.

We would like to express our thanks to Dr. Bogusław Penc for assistance in creating Fig. 12.

Appendix A. Supporting information

Supplementary data associated with this article can be found in the online version at doi:10.1016/j.jallcom.2021.160171.

References

[1] N.L. Gulay, M. Daszkiewicz, Yu.B. Tyvanchuk, Ya.M. Kalychak, D. Kaczorowski, Crystal structure and magnetic properties of the novel compound $Sc_5Pd_2In_4$, J. Alloy. Compd. 750 (2018) 92–95, https://doi.org/10.1016/j.jallcom.2018.03.360

[2] L.D. Sojka, M. Daszkiewicz, B.D. Belan, M.B. Manyako, V.M. Davydov, L.G. Akselrud, Y.M. Kalychak, Crystal structure of $R_5Pd_2In_4$ (R = Y, Tb, Dy, Ho, Er, Tm, Lu), Ukr. Chem. Journ. 74 (2008) 90–94.

[3] V.I. Zaremba, Ya.M. Kalychak, P.Yu. Zavalii, V.A. Bruskov, Crystal structures of the compounds $R_5Ni_2In_4$ (R = Ho, Er, Tm, Lu), Kristallografiya 36 (1991) 1415–1418 (English translated: Sov. Phys. Crystallogr. 36 (1991) 801–803).

[4] C. Ritter, A. Provino, P. Manfrinetti, V.K. Pecharsky, K.A. Gschneidner Jr., S.K. Dhar, Magnetic structures of $R_5Ni_2In_4$ and $R_{11}Ni_4In_9$ (R = Tb and Ho): strong hierarchy in the temperature dependence of the magnetic ordering in the multiple rare-earth sublattices, J. Phys. Condens. Matter 27 (2015) 476001, https://doi.org/10.1088/0953-8984/27/47/476001

[5] A. Provino, Y. Mudryk, D. Paudyal, V. Smetana, P. Manfrinetti, V.K. Pecharsky, K.A. Gschneidner Jr., J.D. Corbett, Crystal structure of $Tb_5Ni_2In_4$ and $Y_5Ni_2In_4$, and magnetic properties of $Dy_5Ni_2In_4$, J. Appl. Phys. 111 (2012) 07E122, https://doi.org/10.1063/1.3673432

[6] Z. Zhang, X. Dong, Q. Wang, L. Li, Investigation of the crystal structure, magnetic phase transition and magnetocaloric effect in $RE_5Ni_2In_4$ (*RE* = Dy, Ho and Er) compounds, Intermetallics 100 (2018) 136–141, https://doi.org/10.1016/j.intermet.2018.06.012

[7] Yu.B. Tyvanchuk, B. Penc, A. Szytuła, A. Zarzycki, Magnetic properties of $Ho_5Ni_2In_4$, Acta Phys. Pol. A 117 (2010) 599–600, https://doi.org/10.12693/APhysPolA.117.599

[8] Ł. Gondek, J. Przewoźnik, J. Czub, Yu. Tyvanchuk, A. Szytuła, A. Arurlaj, Crystal and magnetic properties of $Er_5Ni_2In_4$ at low temperatures, Intermetallics 21 (2012) 10–17, https://doi.org/10.1016/j.intermet.2011.09.007

[9] A. Szytula, Yu. Tyvanchuk, S. Baran, J. Przewoznik, Ya.M. Kalychak, Magnetic and thermal properties of $Tm_5Ni_2In_4$, Intermetallics 43 (2013) 99–102, https://doi.org/10.1016/j.intermet.2013.07.014

[10] A. Szytuła, S. Baran, D. Kaczorowski, W. Sikora, A. Hoser, Magnetic ordering in $Tm_5Ni_2In_4$, J. Alloy. Compd. 617 (2014) 149–153, https://doi.org/10.1016/j.jallcom.2014.07.190

[11] J. Rodríguez-Carvajal, Recent advances in magnetic structure determination neutron by powder diffraction, Phys. B 192 (1993) 55–69, https://doi.org/10.1016/0921-4526(93)90108-I

[12] J. Rodríguez-Carvajal, Recent developments of the program FULLPROF, Newsletter of the Commission for Powder Diffraction of the IUCr 26 (2001) 12–19.

[13] R.D. Shannon, Revised effective ionic radii and systematic studies of interatomic distances in halides and chalcogenides, Acta Cryst. A 32 (1976) 751–767, https://doi.org/10.1107/S0567739476001551

[14] M. Giovannini, H. Michor, E. Bauer, G. Hilscher, P. Rogl, R. Ferro, Structural chemistry, magnetism and thermodynamic properties of R_2Pd_2In, J. Alloy. Compd. 280 (1998) 26–38, https://doi.org/10.1016/S0925-8388(98)00723-3

[15] S. Stein, L. Heletta, R. Pöttgen, Ternary indides $RE_3T_2In_4$ (*RE* = Dy-Tm; *T* = Pd, Ir), Z. Naturforsch. B 73 (2018) 765–772, https://doi.org/10.1515/znb-2018-0091

[16] E.N. Maslen, V.A. Streltsov, N. Ishizawa, A synchrotron X-ray study of the electron density in C-type rare earth oxides, Acta Cryst. B 52 (1996) 414–422, https://doi.org/10.1107/S0108768195013371

[17] S. Baran, A. Szytuła, D. Kaczorowski, F. Damay, Magnetic structures in TmPdIn and TmAgSn, J. Alloy. Compd. 662 (2016) 11–15, https://doi.org/10.1016/j.jallcom.2015.11.200

[18] D.R. Noakes, G.K. Shenoy, The effect of a crystalline electric field on the magnetic transition temperatures of rare-earth rhodium borides, Phys. Lett. A 91 (1982) 35–36, https://doi.org/10.1016/0375-9601(82)90258-4

[19] B.D. Dunlap, L.N. Hall, F. Behroozi, G.W. Crabtree, D.G. Niarchos, Crystal-field effects and the magnetic properties of rare-earth rhodium borides, Phys. Rev. B 29 (1984) 6244–6251, https://doi.org/10.1103/PhysRevB.29.6244

[20] A. Szytuła, S. Baran, J. Przewoźnik, Yu. Tyvanchuk, Ya. Kalychak, Magnetic properties and specific heat data of $R_{11}Ni_4In_9$ (R = Pr, Nd, Sm, Gd and Tb) compounds, J. Alloy. Compd. 601 (2014) 238–244, https://doi.org/10.1016/j.jallcom.2014.02.183

[21] S. Baran, Yu. Tyvanchuk, B. Penc, Ya. Kalychak, A. Hoser, A. Szytuła, Crystal structure and complex magnetic properties of $R_{11}Pd_4In_9$ compounds (R = Y, Gd-Er), Intermetallics 123 (2020) 106837, https://doi.org/10.1016/j.intermet.2020.106837

[22] K.W.H. Stevens, Matrix elements and operator equivalents connected with the magnetic properties of rare earth ions, Proc. Phys. Soc. A 65 (1952) 209–215, https://doi.org/10.1088/0370-1298/65/3/308

[23] I.A. Campbell, Indirect exchange for rare earths in metals, J. Phys. F Met. Phys. 2 (1972) L47–L50, https://doi.org/10.1088/0305-4608/2/3/004

[24] P.G. De Gennes, Interactions indirectes entre couches 4*f* dans les métaux de terres rares, J. Phys. Radium 23 (1962) 510–521, https://doi.org/10.1051/jphysrad:01962002308-9051001